Effective scattering coefficient of the cerebral spinal fluid in adult head models for diffuse optical imaging

Anna Custo, William M. Wells III, Alex H. Barnett, Elizabeth M. C. Hillman, and David A. Boas

An efficient computation of the time-dependent forward solution for photon transport in a head model is a key capability for performing accurate inversion for functional diffuse optical imaging of the brain. The diffusion approximation to photon transport is much faster to simulate than the physically correct radiative transport equation (RTE); however, it is commonly assumed that scattering lengths must be much smaller than all system dimensions and all absorption lengths for the approximation to be accurate. Neither of these conditions is satisfied in the cerebrospinal fluid (CSF). Since line-of-sight distances in the CSF are small, of the order of a few millimeters, we explore the idea that the CSF scattering coefficient may be modeled by any value from zero up to the order of the typical inverse line-of-sight distance, or approximately 0.3 mm^{-1}, without significantly altering the calculated detector signals or the partial path lengths relevant for functional measurements. We demonstrate this in detail by using a Monte Carlo simulation of the RTE in a three-dimensional head model based on clinical magnetic resonance imaging data, with realistic optode geometries. Our findings lead us to expect that the diffusion approximation will be valid even in the presence of the CSF, with consequences for faster solution of the inverse problem.

OCIS codes: 170.6960, 170.3660, 170.5280, 170.6920.

1. Introduction

Diffuse optical imaging (DOI) is a relatively new method used to image blood oxygenation *in vivo*. It uses near-infrared light and has the advantage of low cost and portability. The success of DOI techniques is due to the properties of near-infrared light in biological tissue. The absorption coefficient (μ_a) depends on the total hemoglobin concentration and oxygenation within the tissue; therefore calculating μ_a provides useful information about the physiological conditions of the tissue.[1] For instance, during the past few years DOI has been tested for application to imaging breast cancer[2–9] and brain function.[10–16]

In DOI, near-infrared light is scattered in a medium with optical properties x, and some fluence y is recorded at the detectors' positions. Solving an imaging problem [described as $f(x) = y$; solved for x] requires a good combination of a forward and an inverse model. The forward problem models the process producing the set of measurements [establishing the rules to calculate $f(x)$]. The inverse problem arises when it is necessary to recover an image of the optical properties of the medium from the observed data [i.e., $x = f^{-1}(y)$]. The DOI image reconstruction problem is ill posed; hence the inverse procedure typically involves the use of regularization techniques.[17,18] Because of its relatively poor spatial resolution, DOI is increasingly combined with other imaging techniques, such as magnetic resonance imaging (MRI) and x ray, which provide high-resolution structural information to guide the characterization of the unique physiological information offered by DOI.[8,19–22]

Several papers have been published by Okada *et al.*,[23] Fukui *et al.*,[24] Hayashi *et al.*,[25] Koyama *et al.*,[26] Arridge *et al.*[27,28] Firbank *et al.*,[29] and Hielscher *et al.*[30] that explore a variety of models of light propagation in highly scattering media with properties

A. Custo (custom@csail.mit.edu) is with the Computer Science and Artificial Intelligence Laboratory, Massachusetts Institute of Technology, Cambridge, Massachusetts 02139 and the Athinoula A. Martinos Center for Biomedical Engineering, Massachusetts General Hospital, Harvard Medical School, Charlestown, Massachusetts 02129. W. M. Wells III is with the Computer Science and Artificial Intelligence Laboratory, Massachusetts Institute of Technology, Cambridge, Massachusetts 02139 and the Department of Radiology, Brigham and Women's Hospital, Harvard Medical School, Boston, Massachusetts 02115. A. H. Barnett, E. M. C. Hillman, and D. A. Boas are with the Athinoula A. Martinos Center for Biomedical Engineering, Massachusetts General Hospital, Harvard Medical School, Charlestown, Massachusetts 02129.

Received 4 November 2005; revised 29 December 2005; accepted 3 January 2006; posted 18 January 2006 (Doc. ID 65791).

0003-6935/06/194747-09$15.00/0

similar to those found in the human head. The low-scattering properties of the cerebral spinal fluid (CSF) surrounding the space between the brain and the dura mater[31] have been of particular concern in the development of an accurate photon migration forward problem for the human head because the diffusion equation is known to provide inaccurate solutions under such circumstances.[23,30,31] Controversy has continued as to whether this low-scattering region (often called the void region) affects sensitivity in the underlying brain tissue.[24,32,33] As a result, several papers have been published exploring the implementation of the radiative transport equation[30,34] (RTE) or hybrid combinations of the radiosity equation and the diffusion equation.[25,26] A number of papers have shown that in some idealized geometries the transport equation is necessary to accurately describe photon migration in the presence of a low-scattering region.[25,30,33,35,36] Transport-based modeling approaches, such as Monte Carlo (MC) simulations, typically require excessively long processing times. This can make them unsuitable for use as the forward model in an effective image reconstruction algorithm. It is therefore desirable to adopt a faster alternative forward model with comparable accuracy. A solution of the diffusion equation by finite difference (FD), for instance, offers greater computational speed at the cost of reduced modeling accuracy.[30,37] It has been suggested[23,37] that the diffusion equation may be sufficiently accurate given the folding nature of the low-scattering region between the brain and the skull and the fact that this space is filled with connective tissue and blood vessels.[38]

The irregularity in the thickness of the CSF layer is of particular interest because it limits the average straight-line distance that a photon would travel in the void region. Thus even if the scattering coefficient μ_s' in the void region were zero, an increase in μ_s' up to the value of the inverse typical straight-line distance is expected to cause little change in photon transport. Barnett *et al.*[37] hypothesized that, since the line of sight of light propagation through the CSF is likely to be an average ≤ 3 mm, approximating the CSF reduced scattering coefficient with a value not larger than its inverse (which is $\sim 0.3\ \mathrm{mm}^{-1}$) would not introduce a large error. Therefore keeping the overall goal of rapid diffusion modeling in mind, we conjecture that we can approximate the CSF scattering coefficient with values between 0.1 and $0.3\ \mathrm{mm}^{-1}$ without introducing an error larger than 20%.

DOI can be achieved by using continuous wave (cw), time domain (TD), and frequency domain measurements. TD measurements of functional brain activity have recently been shown to provide dramatically enhanced sensitivity to cortical activation.[39–42] In this paper we consider both cw and TD propagation of light through the human head. We expect that our conclusions about the suitability of a larger scattering coefficient to approximate CSF will extend to frequency domain measurements.

We recently began exploring the use of 3D MRI of the human head as a spatial prior step in an iterative reconstruction process of the optical properties of the different structures in the human head[37] as well as for improving quantitative functional imaging.[22,42] This work required creation of a MRI-based anatomically correct 3D model of the head and brain. In this paper we used MC modeling, which implements the transport equation,[44,45] to accurately simulate light propagation through this MRI-based 3D model of the human head. We simulated both time-resolved and cw measurements to validate our hypothesis of an effective CSF scattering coefficient by measuring the error introduced when using a CSF scattering coefficient larger than a near zero value (we used the reference CSF scattering coefficient of $0.001\ \mathrm{mm}^{-1}$). Given this new larger effective μ_s', the conditions for validity of the diffusion approximation may hold to a much greater degree than previously thought, allowing accurate diffusion solution.

We calculated the deviation from our reference measurements of the photon fluence detected on the surface of the head and of the sensitivity to the brain. The results presented in this paper support our hypothesis that the nonscattering CSF region can be treated with a larger scattering coefficient ($0.3\ \mathrm{mm}^{-1}$) with only a 20% difference in the measurements. This result will also have relevance for the debate on the exact CSF scattering coefficient, since it demonstrates that, as long as it is less than the inverse typical line-of-sight distances, its exact value is not relevant. Thus it is possible in principle that the diffusion equation may provide sufficiently accurate modeling of photon migration through the human head, greatly reducing the computational expense.

2. Methods

A. Head Model and Probe Placement

We used segmented MRI data to create the head geometry that we employed for this study. Within this adult head model we distinguished three tissue types (extracerebral, CSF, and cerebral, as described in Table 1). The whole volume is voxelized in a cube with 128 voxels/side (a total of 128^3 voxels, $2 \times 2 \times 2\ \mathrm{mm}^3$ each). A coronal slice of the 3D head model is shown in Fig. 1 with a voxel size of 1 mm. This voxel size was increased to 2 mm for the simulation, decreasing the simulation run time and the memory requirement. In data not reported we established that this increase in voxel size did not significantly affect the simulated data. The gray diamond and the circles on the surface of the head show the placement of the source and detectors, respectively.

The optical properties provided in Table 1 for each tissue type were taken from the literature.[46–48] The refractive index was the same for all tissues and assumed to be 1, and the scattering anisotropy $g = 0.01$. We chose a value of μ_s' for CSF between 0.001 and $1\ \mathrm{mm}^{-1}$ to test our hypothesis that the value of the CSF scattering coefficient could be mod-

Table 1. Optical Properties of the Adult Head Model

Tissue Type	Reduced Transport Scattering Coefficient (mm^{-1})	Absorption Coefficient (mm^{-1})	Tissue Thickness (mm)
Scalp and skull	0.86	0.019	3–8 (scalp) 7–8 (skull)
CSF	0.001, 0.01, 0.1, 0.2, 0.3, 0.7, 1	0.004	2–4
Gray and white matter	1.11	0.01	4–10 (gray) >40 (white)

eled as the inverse of the average CSF layer thickness.[37] In our model we calculated $\mu_{s,CSF}' = 1/\text{average thickness}_{CSF}$, which gave us a μ_s' of $\sim 0.25\ mm^{-1}$.

For the purpose of this study, we used a linear probe geometry, in which the sources and detectors were positioned along a line on the surface of the head, all placed in the same coronal plane. The probe featured a single source and 25 detectors placed at 12, 14, 16, 18 . . . 60 mm from the source position. The source was located at the top of the head (see Fig. 1). We chose this particular arrangement of optodes to analyze the effect of the CSF scattering coefficient on the measured photon fluence as a function of the separation between the source and the detector. Furthermore, the same probe has been used in similar studies by Okada *et al.*[23]

B. Solution of the Radiative Transport Equation

MC modeling is a simple method that offers a great deal of freedom in defining geometries and optical properties based on the RTE.[44,45] The method models photon trajectories through heterogeneous tissues, reproducing the randomness of each scattering event in a stochastic fashion (a random seed is employed). When a photon is detected, its partial optical path length for each of the tissue types through which it passed is recorded in a history file. MC methods have the disadvantage of being computationally expensive to use while obtaining a good signal-to-noise ratio (SNR) in highly scattering thick tissues. We typically ran 10^9 photons to achieve an appropriate SNR for the results presented in this paper. We ran 11 independent MC simulations of 10^8 photons for each μ_s' configuration so that we could calculate the standard deviation across the independent runs. Each simulation took approximately 12 h (see Boas *et al.*[45] for more details). By recording the path length of each photon, our MC data could be converted to cw or TD.

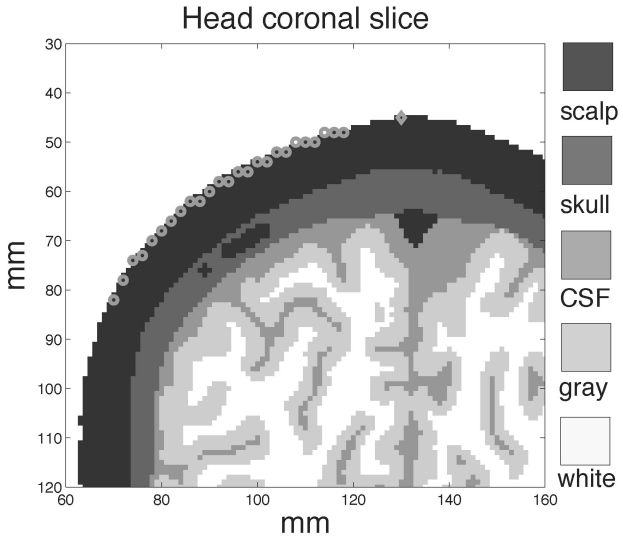

Fig. 1. Head geometry and probe placement. The gray diamond on the top of the head indicates the position of the single source and the gray circles show the position of the 25 detectors.

C. Calculation of the Total Fluence in Time Domain and Continuous Wave

To consider the time-resolved problem from the data recorded by the MC simulation we calculated the temporal point spread function by using Eq. (2) from Ref. 45:

$$\Phi_j(t_i) = \frac{1}{N_j(t_i)\Delta t} \sum_{l=1}^{N_j(t_i)} \prod_{m=1}^{N_R} \exp(-\mu_{a,m} L_{j,l,m}), \qquad (1)$$

where $\Phi_j(t_i)$ is the measured photon fluence at detector j, $N_j(t_i)$ is the number of photons collected at detector j in a time gate of width Δt centered at time t_i, $\exp(-\mu_{a,m} L_{j,l,m})$ accounts for the effects of absorption in each region in which $L_{j,l,m}$ is the path length of photon l through region m, and the photon migration time is related to the photon path length by the speed of light in the medium. N_R is the number of regions through which the photons migrate. The cw fluence is calculated by averaging over the time index i.

D. Calculation of Partial Optical Path Length Factor

Tissue scattering causes the photons to travel a greater distance than the geometric distance between the source and the detector. The partial path length factor (PPF) of light through each of the tissue types is defined as[24,38,39,49]

$$\text{PPF}_m = \partial \text{OD} / \partial \mu_{a,m}, \qquad (2)$$

where $\text{OD} = -\ln(\Phi/\Phi_0)$, Φ/Φ_0 is given by Eq. (1), and Φ_0 is the incident number of photons. The partial path length is thus easily derived from Eq. (1):

$$\text{PPF}_{j,m} = \frac{\sum_{l=1}^{N_j(t_i)} \prod_{m=1}^{N_S} L_{j,l,m} \exp(-\mu_{a,m} L_{j,l,m})}{\sum_{l=1}^{N_j(t_i)} \prod_{m=1}^{N_R} \exp(-\mu_{a,m} L_{j,l,m})}. \qquad (3)$$

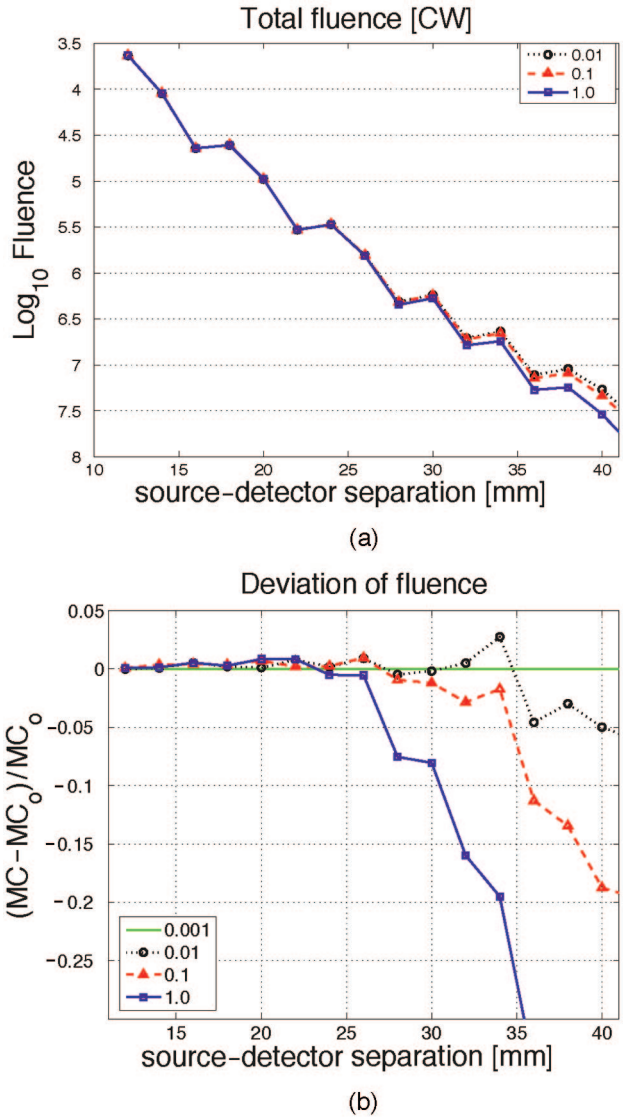

Fig. 2. (Color online) (a) Total detected fluence simulated with Monte Carlo in cw. (b) Relative fluence in cw calculated with respect to MC_o, which is the MC prediction when $\mu_{s,CSF}' = 0.001$ mm^{-1}.

3. Results

A. Fluence and Partial Path Length for Continuous Wave

In Fig. 2 we show the total measured fluence versus the source–detector separation for different $\mu_{s,CSF}'$ [Fig. 2(a)] and the fractional difference relative to $\mu_{s,CSF}' = 0.001$ mm^{-1} [Fig. 2(b)]. The total fluence is normalized by the incident fluence, i.e., the total number of photons launched in the MC simulation. We see that the detected fluence varies little when the $\mu_{s,CSF}' \leq 0.1$ mm^{-1} but that a significant difference occurs at larger $\mu_{s,CSF}'$ for separations greater than 25 mm. In Fig. 2(b) we see that at small separations (12–22 mm) the fractional difference for increasing $\mu_{s,CSF}'$ is less than 2%, becoming significant (>20%) at larger separations (>32 mm) when $\mu_{s,CSF}'$ is 1.0 mm^{-1}. This is to be expected because smaller separations are predominantly sensitive to the scalp–skull and therefore do not probe the CSF layer.

In Fig. 3(a) we show the cw partial path length for the scalp–skull region and the brain region versus the source–detector separation for different scattering coefficients in the CSF region. The results show that the sensitivity of the measurement to absorption changes does not change as μ_s' in the CSF space increases from 0.01 to 0.1 mm^{-1}, but that a change is observed with $\mu_s' = 1.0$ mm^{-1}. This is consistent with the hypothesis that the sensitivity will change as the scattering length becomes smaller than the typical line-of-sight distance through the CSF, which is approximately 3 mm in our model.

In Figs. 3(b) and 3(c) we plotted the fractional difference in the PPF for the scalp–skull region and the brain region relative to that when $\mu_{s,CSF}' = 0.001$ mm^{-1}. In Fig. 3(b) we observe a difference greater than 3% at larger separations (>30 mm) for a CSF model with $\mu_s' = 1.0$ mm^{-1}, and a difference less than 1% for $\mu_{s,CSF}' = 0.1$ and 0.01 mm^{-1}. Figure 3(c) shows the same fractional difference observed in the brain. In the brain, even at small separations, we observed a large difference only when $\mu_{s,CSF}' = 1.0$ mm^{-1}, increasing from 20% to 47% as the separation increases. For the smaller $\mu_{s,CSF}'$ we observed differences less than 10% at all separations.

To investigate the variation in more detail, we plotted in Figs. 4 and 5 the deviation in detected photon fluence at the surface of the scalp (Fig. 4) and the deviation in the partial path length in the scalp–skull and brain (Fig. 5) versus μ_s' of the CSF at source–detector separations of 20, 30, and 40 mm. These results show that a change greater than 20% is not observed until $\mu_s' > 0.3$ mm^{-1}, except at a 40 mm separation. We believe that the large discrepancy observed at 40 mm is due to the weakness of the signal reaching the far detectors. These results support our hypothesis that we can treat this voidlike region with a larger scattering coefficient ($0.1 < \mu_s' < 0.3$ mm^{-1}) and obtain similar results (errors between 10% and 20% for cw measurements with a source–detector spacing of <40 mm).

We also note from Figs. 3(a) and 5 that the brain PPF, which corresponds to the sensitivity of the cw measurement to absorption changes in the brain, is higher when the CSF μ_s' is low than when the CSF μ_s' matches that of the brain.

B. Fluence and Partial Path Length in the Time Domain

We further explored this result for time-resolved photon migration. In Fig. 6(a) we show how the partial path length varied with the photon transit time in the medium. These results confirm what we have seen in cw, that is, the time-resolved fluence is approximately the same when $\mu_{s,CSF}'$ is less than 0.1 mm^{-1} but a significant difference is observed for a larger scattering coefficient. In Fig. 6(b) we quantified this change relative to the fluence when $\mu_{s,CSF}' = 0.001$ mm^{-1} and observed a greater than 50% de-

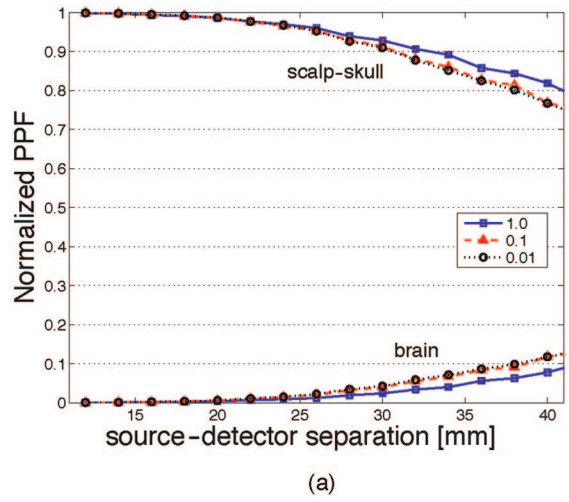

(a)

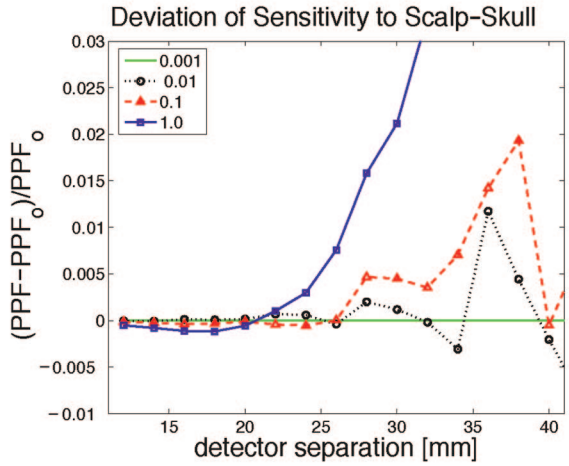

(b)

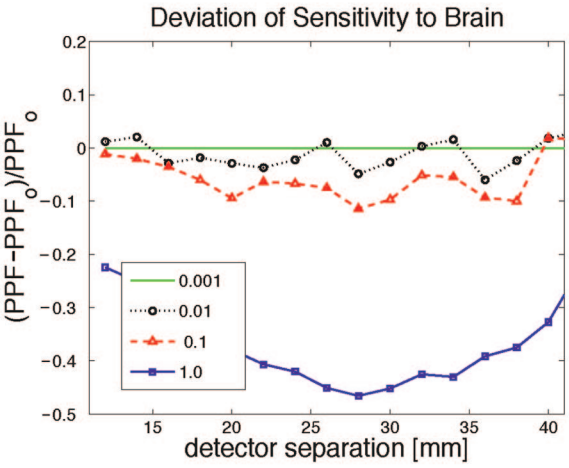

(c)

Fig. 3. (Color online) (a) MC normalized path length factor calculated versus separation for three different $\mu_{s,CSF}'$: 0.01, 0.1, and 1.0 mm^{-1} in cw. The PPF is normalized by the total sensitivity to all tissue types. MC measure of relative sensitivity to (b) scalp–skull layer and (c) brain versus separation when varying $\mu_{s,CSF}'$ in cw ($\mu_{s,CSF}'$ = 0.01, 0.1, and 1.0 mm^{-1}). The error is calculated with respect to PPF$_o$, which is the MC prediction of PPF when $\mu_{s,CSF}'$ = 0.001 mm^{-1}.

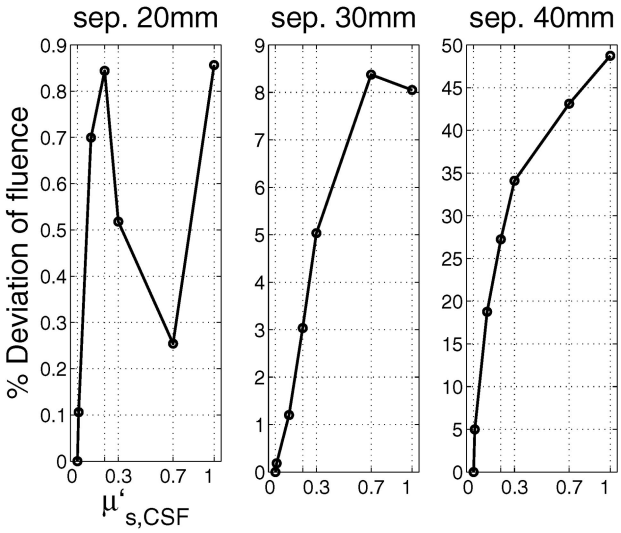

Fig. 4. Fluence changes as a function of $\mu_{s,CSF}'$. CSF scattering coefficient varies from 0.001 to 1.0 mm^{-1}. The data are calculated via MC simulations in cw using $\mu_{s,CSF}'$ values of 0.001, 0.01, 0.1, 0.2, 0.3, 0.7, and 1.0.

viation for $\mu_{s,CSF}'$ = 1.0 mm^{-1} and a mostly less than 8% deviation when $\mu_{s,CSF}'$ = 0.1 and 0.01 mm^{-1}.

In Fig. 7 we explored how the CSF scattering coefficient affects the partial path length in the superficial layers and the brain versus time delay. The absolute partial path length in Fig. 7(a) shows that no difference is observed for $\mu_{s,CSF}'$ = 0.1 and 0.01 mm^{-1} but that a difference is observed when μ_s' is further increased to 1.0 mm^{-1}. The deviation with increasing $\mu_{s,CSF}'$ relative to a $\mu_{s,CSF}'$ of 0.001 mm^{-1} is shown in Figs. 7(b) and 7(c) for the superficial and brain re-

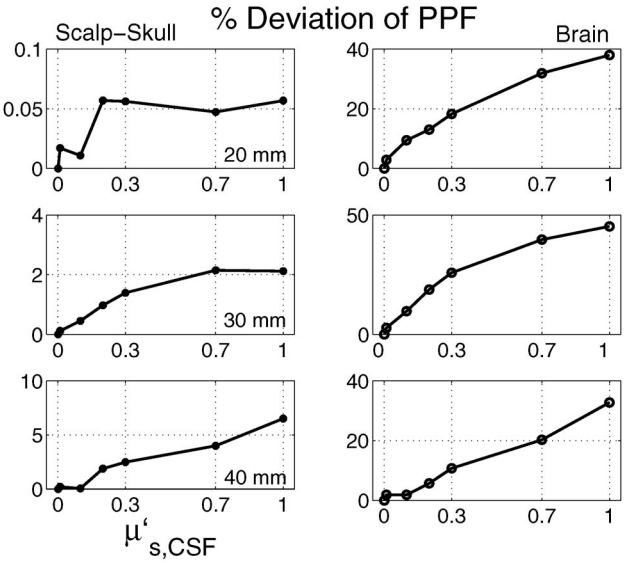

Fig. 5. Partial path length absolute changes as a function of $\mu_{s,CSF}'$ scattering coefficient varies from 0.001 to 1.0 mm^{-1} taking values of 0.001, 0.01, 0.1, 0.2, 0.3, 0.7, and 1.0, and the PPF is simulated with MC in cw. Results are shown for separations of 20, 30, and 40 mm.

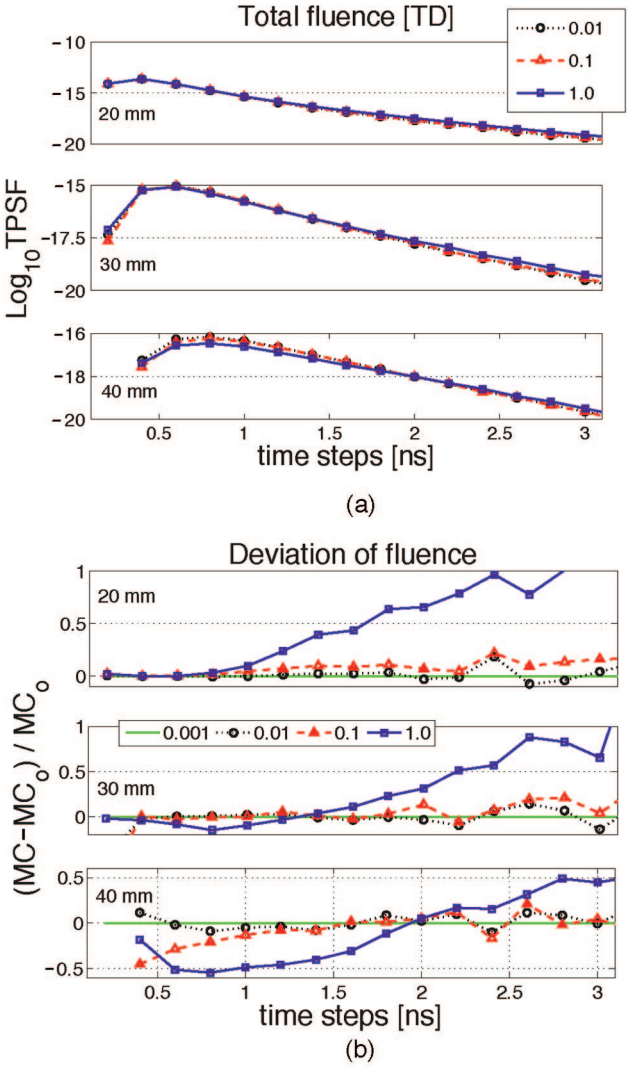

Fig. 6. (Color online) (a) Temporal point spread function predicted by MC and (b) its relative error with respect to the reference measurement MC_o, simulated with $\mu_{s,CSF}' = 0.001\ mm^{-1}$. Results are shown for separations of 20, 30, and 40 mm.

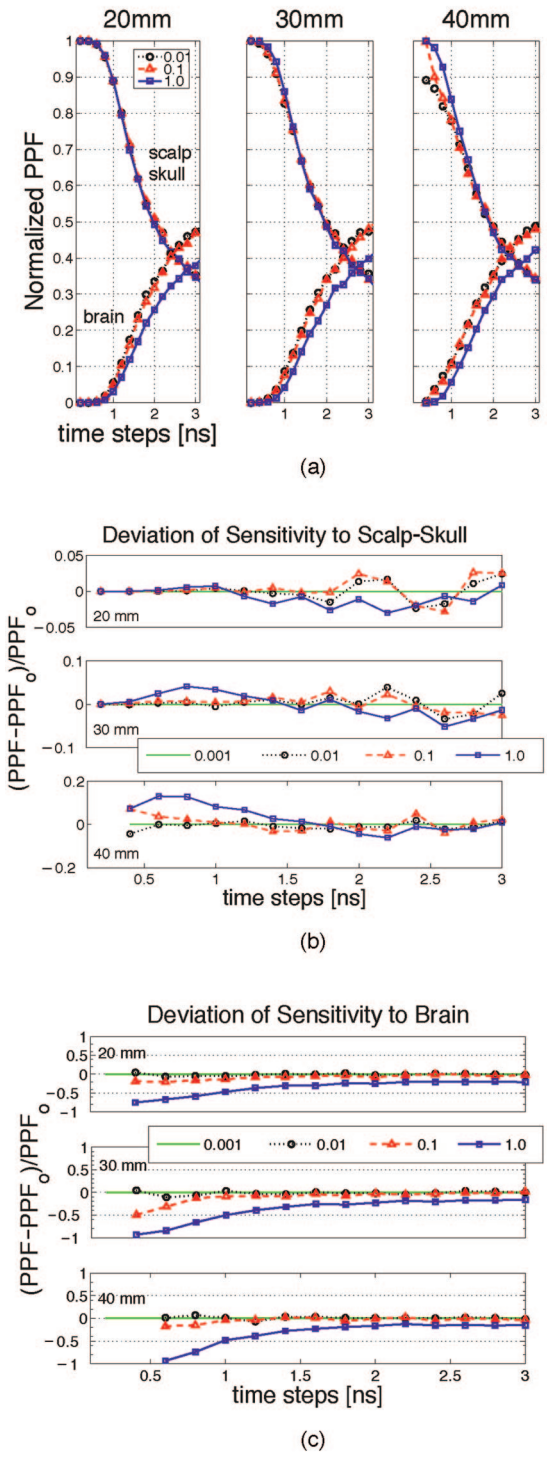

Fig. 7. (Color online) (a) Monte Carlo prediction of the optical pathlength factor at three $\mu_{s,CSF}' = 0.01$, 0.1, and $1.0\ mm^{-1}$ versus time delay normalized by the total PPF. Results are shown for separations of 20, 30, and 40 mm. (b) Relative sensitivity to absorption changes in the scalp–skull layer when $\mu_{s,CSF}' = 0.01$, 0.1, and $1.0\ mm^{-1}$ versus time delay as predicted by Monte Carlo. The reference measure of sensitivity to scalp–skull is given by simulating PPF when $\mu_{s,CSF}'$ is $0.001\ mm^{-1}$. (c) Time-resolved Monte Carlo predictions of the relative sensitivity to absorption changes in the brain when $\mu_{s,CSF}'$ assumes the values of 0.01, 0.1 and $1.0\ mm^{-1}$. The reference measure of sensitivity to brain is given by simulating PPF when $\mu_{s,CSF}'$ is $0.001\ mm^{-1}$. Results are shown for separations of 20, 30, and 40 mm.

gions, respectively. Little deviation is observed in the superficial scalp–skull region since the deviation is never larger than 15%. A more significant difference is observed for the brain, where the partial path length is underestimated by 20%–50% for $\mu_{s,CSF}' = 1.0\ mm^{-1}$, whereas the error is less than 20% when $\mu_{s,CSF}' < 0.3\ mm^{-1}$. In all cases, the error is greater at the earliest photon migration times when brain sensitivity is weakest.

Figures 8 and 9 show the deviation in the detected fluence and PPF, respectively, versus $\mu_{s,CSF}'$ at 20, 30, and 40 mm at a time delay of 2 ns, where we see that changes greater than 20% occur only when $\mu_s' > 0.3\ mm^{-1}$. These results further support the observation that the CSF layer can be accurately characterized by a scattering coefficient value between 0 and $\sim 0.3\ mm^{-1}$ and still provide detected

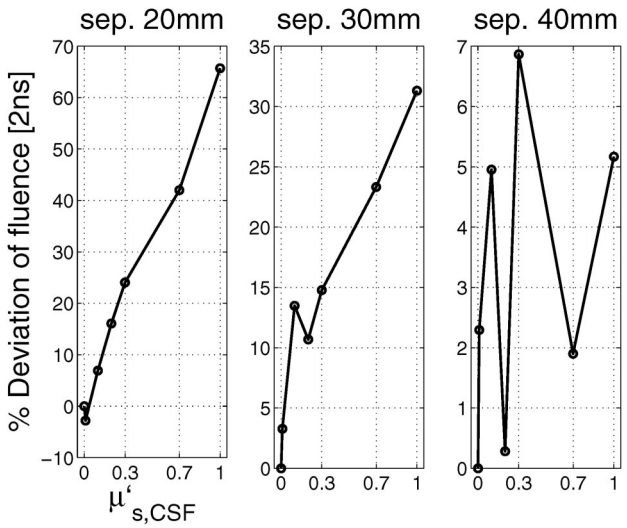

Fig. 8. Fluence changes as a function of $\mu_{s,CSF}'$ for different separations at a time delay of 2 ns. CSF scattering coefficient varies between 0.001 and 1.0 mm^{-1}.

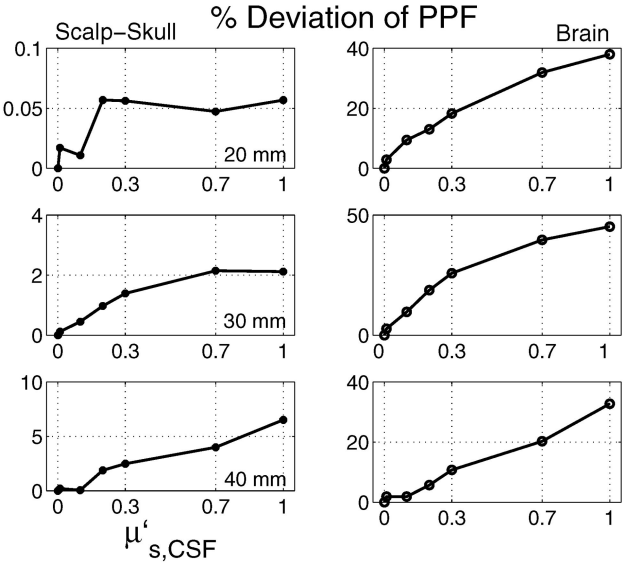

Fig. 9. Absolute changes in the partial optical path length versus $\mu_{s,CSF}'$ at source–detector separations of 20, 30, and 40 mm for a time delay of 2 ns.

fluence and brain sensitivity within an acceptable approximation error (between 10% and 20%).

As with the cw results, we note that for the TD measurements the partial path length in the brain also increases when the CSF reduced scattering coefficient is low [see Figs. 7(a) and 9]. Also, importantly, sensitivity to absorption changes in the brain is significantly enhanced at time delays greater than 1.5 ns with respect to cw sensitivity measurements [compare Figs. 3(a) and 7(a)].

4. Conclusions

We performed extensive simulation studies to quantify the deviation in photon migration measurements and sensitivity to brain activity given a range of CSF scattering coefficient values. Through an analysis of total fluence and partial optical path length using MC simulations in an accurate MRI-based 3D head geometry, we found that the CSF scattering coefficient can increase up to the inverse of its typical thickness without significant variation from a near zero scattering coefficient. The results support our initial hypothesis that an effective CSF scattering coefficient of approximately 0.3 mm^{-1} can be used. Under these circumstances it may be possible to obtain accurate solutions of the forward problem with diffusion approximation. The advantage of using diffusion approximation is that we can utilize faster algorithms to simulate photon migration in the adult head.

Our results also suggest that low-scattering CSF increases DOI measurement sensitivity to brain activity in contrast to previous studies that assumed a simplified smooth CSF layer.[32,42,50,51] CSF may change the depth sensitivity profile, but this does not mean that the signal from the cortex is decreased in the presence of low-scattering CSF. We hypothesize that the presence of the CSF layer has the effect of concentrating measurement sensitivity to the more superficial layers of the cortex, but that the overall sensitivity to cortical hemodynamics is not adversely affected.

In conclusion, our results indicate the following:

(i) Using a diffusion model with a CSF reduced scattering coefficient of approximately 0.3 mm^{-1} leads to measurements with errors no larger than 20%, for both TD and cw.

(ii) The sensitivity of DOI measurements to cortical activity is not adversely affected by the presence of CSF in a realistic 3D head geometry.

(iii) TD measurements can further reduce the effect of the CSF layer by increasing the sensitivity to deeper tissues, in agreement with the previous findings of Steinbrink *et al.*,[47] Montcel *et al.*,[41] and Okada and Delpy.[42]

We thank Jon Stott for useful conversations and guidance in the early stages of this work. This work was supported by the National Institutes of Health, (P41-RR14075 and R01-EB002482) and the National Science Foundation under grant IIS 9610249.

References

1. V. Chernomordik, D. W. Hattery, D. Grosenick, H. Wabnitz, H. Rinneberg, K. T. Moesta, P. M. Schlag, and A. Gandjbakhche, "Quantification of optical properties of a breast tumor using random walk theory," J. Biomed. Opt. **7,** 80–87 (2002).
2. N. Shah, A. E. Cerussi, D. Jakubowski, D. Hsiang, J. Butler, and B. J. Tromberg, "The role of diffuse optical spectroscopy in the clinical management of breast cancer," Dis. Markers **19,** 95–105 (2003).
3. R. Choe, A. Corlu, K. Lee, T. Durduran, S. D. Konecky, M. Grosicka-Koptyra, S. R. Arridge, B. J. Czerniecki, D. L. Fraker, A. DeMichele, B. Chance, M. A. Rosen, and A. G. Yodh, "Diffuse optical tomography of breast cancer during neoadjuvant chemotherapy: a case study with comparison to MRI," Med. Phys. **32,** 1128–1139 (2005).
4. X. Intes, J. Ripoll, Y. Chen, S. Nioka, A. G. Yodh, and B. Chance, "In vivo continuous-wave optical breast imaging en-

hanced with Indocyanine Green," Med. Phys. **30,** 1039–1147 (2003).
5. P. Taroni, G. Danesini, A. Torricelli, A. Pifferi, L. Spinelli, and R. Cubeddu, "Clinical trial of time-resolved scanning optical mammography at 4 wavelengths between 683 and 975 nm," J. Biomed. Opt. **9,** 464–473 (2004).
6. D. Grosenick, H. Wabnitz, K. T. Moesta, J. Mucke, M. Moller, C. Stroszczynski, J. Stossel, B. Wassermann, P. M. Schlag, and H. Rinneberg, "Concentration and oxygen saturation of haemoglobin of 50 breast tumours determined by time-domain optical mammography," Phys. Med. Biol. **49,** 1165–1181 (2004).
7. S. Srinivasan, B. W. Pogue, S. Jing, H. Dehghani, C. Kogel, S. Soho, J. J. Gibson, T. D. Tosteson, S. P. Poplack, and K. D. Paulsen, "Interpreting hemoglobin and water concentration, oxygen saturation, and scattering measured in vivo by near-infrared breast tomography," Proc. Natl. Acad. Sci. U.S.A. **100,** 12349–12354 (2003).
8. A. Li, E. L. Miller, M. E. Kilmer, T. J. Brukilacchio, T. Chaves, J. Stott, Q. Zhang, T. Wu, M. Chorlton, R. H. Moore, D. B. Kopans, and D. A. Boas, "Tomographic optical breast imaging guided by three-dimensional mammography," Appl. Opt. **42,** 5181–5190 (2003).
9. M. A. Franceschini, K. T. Moesta, S. Fantini, G. Gaida, E. Gratton, H. Jess, W. W. Mantulin, M. Seeber, P. M. Schlag, and M. Kaschke, "Frequency-domain techniques enhance optical mammography: initial clinical results," Proc. Natl. Acad. Sci. U.S.A. **94,** 6468–6473 (1997).
10. A. Villringer, J. Planck, C. Hock, L. Schleinkofer, and U. Dirnagl, "Near infrared spectroscopy (NIRS): a new tool to study hemodynamic changes during activation of brain function in human adults," Neurosci. Lett. **154,** 101–104 (1993).
11. Y. Hoshi and M. Tamura, "Detection of dynamic changes in cerebral oxygenation coupled to neuronal function during mental work in man," Neurosci. Lett. **150,** 5–8 (1993).
12. M. A. Franceschini, S. Fantini, J. H. Thompson, J. P. Culver, and D. A. Boas, "Hemodynamic evoked response of the sensorimotor cortex measured non-invasively with near infrared optical imaging," Psychophysiology **40,** 548–560 (2003).
13. H. Koizumi, T. Yamamoto, A. Maki, Y. Yamashita, H. Sato, H. Kawaguchi, and N. Ichikawa, "Optical topography: practical problems and new applications," Appl. Opt. **42,** 3054–3062 (2003).
14. M. Pena, A. Maki, D. Kovacic, G. Dehaene-Lambertz, H. Koizumi, F. Bouquet, and J. Mehler, "Sounds and silence: an optical topography study of language recognition at birth," Proc. Natl. Acad. Sci. U.S.A. **100,** 11702–11705 (2003).
15. E. Gratton, V. Toronov, U. Wolf, M. Wolf, and A. Webb, "Measurement of brain activity by near-infrared light," J. Biomed. Opt. **10,** 011008 (2005).
16. T. Wilcox, H. Bortfeld, R. Woods, E. Wruck, and D. A. Boas, "Using near-infrared spectroscopy to assess neural activation during object processing in infants," J. Biomed. Opt. **10,** 011010 (2005).
17. S. R. Arridge, "Optical tomography in medical imaging," Inverse Probl. **15,** 41–93 (1999).
18. M. Bertero and P. Boccacci, *Introduction to Inverse Problems in Imaging* (Institute of Physics, 1998).
19. R. L. Barbour, H. L. Graber, J. Change, S. S. Barbour, P. C. Koo, and R. Aronson, "MRI-guided optical tomography: prospects and computation for a new imaging method," IEEE Comput. Sci. Eng. **2,** 63–77 (1995).
20. B. W. Pogue and K. D. Paulsen, "High-resolution near-infrared tomographic imaging simulations of the rat cranium by use of a priori magnetic resonance imaging structural information," Opt. Lett. **23,** 1716–1718 (1998).
21. V. Ntziachristos, A. G. Yodh, M. Schnall, and B. Chance, "MRI-guided diffuse optical spectroscopy of malignant and benign breast lesions," Neoplasia **4,** 347–354 (2002).
22. D. A. Boas and A. M. Dale, "Simulation study of magnetic resonance imaging-guided cortically constrained diffuse optical tomography of human brain function," Appl. Opt. **44,** 1957–1968 (2005).
23. E. Okada, M. Firbank, M. Schweiger, S. R. Arridge, M. Cope, and D. T. Delpy, "Theoretical and experimental investigation of near-infrared light propagation in a model of the adult head," Appl. Opt. **36,** 21–31 (1997).
24. Y. Fukui, Y. Ajichi, and E. Okada, "Monte Carlo prediction of near-infrared light propagation in realistic adult and neonatal head models," Appl. Opt. **42,** 2881–2887 (2003).
25. T. Hayashi, Y. Kashio, and E. Okada, "Hybrid Monte Carlo-diffusion method for light propagation in tissue with a low-scattering region," Appl. Opt. **42,** 2888–2896 (2003).
26. T. Koyama, A. Iwasaki, Y. Ogoshi, and E. Okada, "Practical and adequate approach to modeling light propagation in an adult head with low-scattering regions by use of diffusion theory," Appl. Opt. **44,** 2094–2103 (2005).
27. S. R. Arridge, M. Schweiger, M. Hiraoka, and D. T. Delpy, "A finite element approach for modeling photon transport in tissue," Med. Phys. **20,** 299–309 (1993).
28. S. R. Arridge, H. Dehghani, M. Schweiger, and E. Okada, "The finite element model for the propagation of light in scattering media: a direct method for domains with nonscattering regions," Med. Phys. **27,** 252–264 (2000).
29. M. Firbank, S. R. Arridge, M. Schweiger, and D. T. Delpy, "An investigation of light transport through scattering bodies with non-scattering regions," Phys. Med. Biol. **41,** 767–783 (1996).
30. A. H. Hielscher, R. E. Alcouffe, and R. L. Barbour, "Comparison of finite-difference transport and diffusion calculations for photon migration in homogeneous and heterogeneous tissues," Phys. Med. Biol. **43,** 1285–1302 (1998).
31. E. M. C. Hillman, *Experimental and theoretical investigations of near infrared tomographic imaging methods and clinical applications* (University College London, 2002).
32. H. Dehghani, S. R. Arridge, M. Schweiger, and D. T. Delpy, "Optical tomography in the presence of void regions," J. Opt. Soc. Am. A **17,** 1659–1670 (2000).
33. E. Okada and D. T. Delpy, "Effect of discrete scatterers in CSF layer on optical path length in the brain," in *Photon Migration, Diffuse Spectroscopy, and Optical Coherence Tomography: Imaging and Functional Assessment*, S. Andersson-Engels and J. G. Fujimoto, eds., Proc. SPIE **4160,** 196–203 (2000).
34. G. Bal and K. Ren, "Generalized diffusion model in optical tomography with clear layers," J. Opt. Soc. A **20,** 2355–2364 (2003).
35. J. D. Riley, S. R. Arridge, Y. Chrysanthou, H. Dehghani, E. M. Hillman, and M. Schweiger, "Radiosity diffusion model in 3D," in *Photon Migration, Optical Coherence Tomography, and Microscopy*, S. Andersson-Engels and M. F. Kaschke, eds., Proc. SPIE **4431,** 153–164 (2001).
36. H. Dehghani, D. T. Delpy, and S. R. Arridge, "Photon migration in non-scattering tissue and the effects on image reconstruction," Phys. Med. Biol. **44,** 2897–2906 (1999).
37. A. H. Barnett, J. P. Culver, A. G. Sorensen, A. Dale, and D. A. Boas, "Robust inference of baseline optical properties of the human head with 3D segmentation from magnetic resonance imaging," Appl. Opt. **42,** 3095–3108 (2003).
38. E. Okada and D. T. Delpy, "Near-infrared light propagation in an adult head model. I. Modeling of low-level scattering in the cerebrospinal fluid layer," Appl. Opt. **42,** 2906–2914 (2003).
39. K. Uludag, M. Kohl, J. Steinbrink, H. Obrig, and A. Villringer, "Cross talk in the Lambert-Beer calculation for near-infrared wavelengths estimated by Monte Carlo simulations," J. of Biomed. Opt. **7,** 51–59 (2002).
40. J. Selb, J. J. Stott, M. A. Franceschini, A. G. Sorenson, and

D. A. Boas, "Improved sensitivity to cerebral dynamics during brain activation with a time-gated optical system: analytical model and experimental validation," J. Biomed. Opt. **10,** 011013 (2005).
41. B. Montcel, R. Chabrier, and P. Poulet, "Detection of cortical activation with time-resolved diffuse optical methods," Appl. Opt. **44,** 1942–1947 (2005).
42. E. Okada and D. T. Delpy, "Effect of a nonscattering layer on time-resolved photon migration paths, in *Photon Propagation in Tissues IV*, D. A. Benaron, B. Chance, M. Ferrari, and M. Kohl-Bareis, eds., Proc. SPIE **3566,** 2–9 (1998).
43. D. A. Boas, A. M. Dale, and M. A. Franceschini, "Diffuse optical imaging of brain activation: approaches to optimizing image sensitivity, resolution, and accuracy," Neuroimage **23,** S275–288 (2004).
44. L. Wang, S. L. Jacques, and L. Zheng, "MCML-Monte Carlo modeling of light transport in multi-layered tissues," Comput. Methods Programs Biomed. **47,** 131–146 (1995).
45. D. A. Boas, J. P. Culver, J. J. Stott, and A. K. Dunn, "Three dimensional Monte Carlo code for photon migration through complex heterogeneous media including the adult human head," Opt. Express **10,** 159–170 (2002).
46. D. A. Boas, G. Strangman, J. P. Culver, R. D. Hoge, G. Jasdzewski, R. A. Poldrack, B. R. Rosen, and J. B. Mandeville, "Can the cerebral metabolic rate of oxygen be estimated with near-infrared spectroscopy?" Phys. Med. Biol. **48,** 2405–2418 (2003).
47. J. Steinbrink, H. Wabnitz, H. Obring, A. Villringer, and H. Rinneberg, "Determining changes in NIR absorption using a layered model of the human head," Phys. Med. Biol. **46,** 879–896 (2001).
48. G. Strangman, M. A. Franceschini, and D. A. Boas, "Factors affecting the accuracy of near-infrared spectroscopy concentration calculations for focal changes in oxygenation parameters," Neuroimage **18,** 865–879 (2003).
49. E. Okada, M. Schweiger, S. R. Arridge, M. Firbank, and D. T. Delpy, "Experimental validation of Monte Carlo and finite-element methods for the estimation of the optical path length in inhomogeneous tissue," Appl. Opt. **35,** 3362–3371 (1996).
50. H. Dehghani and D. T. Delpy, "Near-infrared spectroscopy of the adult head: Effect of scattering and absorbing obstructions in the cerebrospinal fluid layer on light distribution in the tissue," Appl. Opt. **39,** 4721–4729 (2000).
51. S. Takahshi and Y. Yamada, "Simulation of 3D light propagation in a layered head model including a clear CSF layer," OSA Trends Opt. Photonics Ser. **21,** 2–6 (1998).